



## Leaching mechanisms of industrial powders of spent nickel metal hydride batteries in a pilot-scale reactor

Margot Zielinski, Laurent Cassayre, Philippe Destrac, Nicolas Coppey, Gilles Garin, Béatrice Biscans

### ► To cite this version:

Margot Zielinski, Laurent Cassayre, Philippe Destrac, Nicolas Coppey, Gilles Garin, et al.. Leaching mechanisms of industrial powders of spent nickel metal hydride batteries in a pilot-scale reactor. ChemSusChem, 2020, 13 (3), pp.616-628. 10.1002/cssc.201902640 . hal-02770455

**HAL Id: hal-02770455**

**<https://hal.science/hal-02770455>**

Submitted on 4 Jun 2020

**HAL** is a multi-disciplinary open access archive for the deposit and dissemination of scientific research documents, whether they are published or not. The documents may come from teaching and research institutions in France or abroad, or from public or private research centers.

L'archive ouverte pluridisciplinaire **HAL**, est destinée au dépôt et à la diffusion de documents scientifiques de niveau recherche, publiés ou non, émanant des établissements d'enseignement et de recherche français ou étrangers, des laboratoires publics ou privés.



## Open Archive Toulouse Archive Ouverte





OATAO is an open access repository that collects the work of Toulouse researchers and makes it freely available over the web where possible

This is an author's version published in: <https://oatao.univ-toulouse.fr/26082>

### Official URL:

<https://doi.org/10.1002/cssc.201902640>

### To cite this version:

Zielinski, Margot  and Cassayre, Laurent  and Destrac, Philippe  and Coppey, Nicolas and Garin, Gilles and Biscans, Béatrice  *Leaching mechanisms of industrial powders of spent nickel metal hydride batteries in a pilot-scale reactor*. (2020) ChemSusChem, 13 (3). 616-628. ISSN 1864-5631.

Any correspondence concerning this service should be sent to the repository administrator: [tech-oatao@listes-diff.inp-toulouse.fr](mailto:tech-oatao@listes-diff.inp-toulouse.fr)

# Leaching Mechanisms of Industrial Powders of Spent Nickel Metal Hydride Batteries in a Pilot-Scale Reactor

Margot Zielinski,<sup>[a, b]</sup> Laurent Cassayre,<sup>[a]</sup> Philippe Destrac,<sup>[a]</sup> Nicolas Coppey,<sup>[b]</sup> Gilles Garin,<sup>[b]</sup> and Béatrice Biscans<sup>\*[a]</sup>

In view of a sustainable recycling process, the leaching mechanisms of nickel and rare-earth elements (REEs) contained within industrial samples of spent nickel metal hydride battery powders were investigated in HCl and H<sub>2</sub>SO<sub>4</sub> under mild temperature (25–60 °C) and pH (3–5.5). First, in-depth characterization of the heterogeneous battery powder was carried out with powder XRD, SEM, electron probe microanalyzer wavelength-dispersive spectroscopy (EPMA-WDS) quantitative analyses of individual particles, and inductively coupled plasma optical emission spectrometry (ICP-OES) elemental analysis. An un-

usual result is the identification of particles that exhibit a core-shell structure, which is related to anode active mass aging mechanisms. Then, a leaching study in a 10 L pilot-scale reactor demonstrated the selective dissolution of REEs, with respect to nickel, at pH 3, which is attributed to 1) the kinetic inhibition of nickel metal dissolution, and 2) the specific core-shell structure of aged mischmetal particles. Furthermore, the use of H<sub>2</sub>SO<sub>4</sub> led to coprecipitation of lanthanide-alkali double sulfates and nickel salts.

## Introduction

Securing access to specialty metals required for high-performance technologies and energy materials has raised environmental and economic concerns in the past decade. Avoiding risks of supply shortages has become a major challenge for highly import-dependent economies, such as the EU.<sup>[1]</sup> This is particularly true for light rare-earth elements (REEs), for which China supplies over 95 % of the world's production, according to the 2017 European Commission report on Critical Raw Materials.<sup>[1]</sup> Developing traditional mine production of such critical minerals in the EU depends on long-term investment projects that are not flexible enough towards rapid changes in market demands.<sup>[1]</sup> On the other hand, recycling of waste electric and electronic equipment (WEEE) or renewable energy materials in the EU can serve as an attractive secondary source of raw materials. For instance, the inner content of nickel metal hydride (NiMH) batteries, which are mainly used for hybrid or pure electric vehicles (HEV or PEV), consists of about 50 wt% nickel<sup>[2]</sup> and 15 wt% REEs.<sup>[3]</sup> More than 1.8 million HEV battery units were sold worldwide in 2016,<sup>[4]</sup> with an average battery collection rate of 44 % in the EU that same year,<sup>[5]</sup> and thus, assuring a significant feed for the recycling market. However, the

contribution of recycling to the market demand for critical materials is still relatively low because it is not yet technically nor economically feasible at the industrial scale.<sup>[6]</sup> As a result, the end-of-life recycling rate of REEs is below 3%<sup>[1,7]</sup> and the end-of-life recycling input rate of nickel is only 25%.<sup>[8]</sup> The 50 wt% recycling efficiency target to be achieved for NiMH batteries, as described by the European Directive (2006/66/EC), makes it necessary for industries to develop more efficient and sustainable recycling schemes, and opens up new possibilities for urban mining.<sup>[8]</sup>

NiMH batteries are made up of four main components: an iron- or aluminum-based outer casing; anode and cathode current collectors, upon which active electrode powders are deposited by using binders; an alkaline electrolyte, such as KOH; and a microporous polymer separator.<sup>[9–12]</sup> The cathode current collector consists of a dense metallic nickel mesh, whereas the cathode active mass is made of spherical particles of either nickel hydroxide  $\beta$ -Ni(OH)<sub>2</sub> or oxyhydroxide NiO(OH), depending on the state of charge of the battery.<sup>[13,14]</sup> The anode typically contains a nickel-plated steel support as the current collector<sup>[13]</sup> and an active mass consisting of a hydride alloy of varying compositions. The structure of hydrogen storage alloys can either be AB<sub>5</sub>, in which A=La, Nd, Pr, Ce, or Y and B=Ni, Co, Mn, or Al; AB<sub>2</sub>, in which A=Ti or Zr and B=Ni, Co, Mn, Al, V, Cr, or Sn; or A<sub>2</sub>B<sub>7</sub>, in which A=Nd or Mg and B=Ni or Al.<sup>[13,15]</sup> Such an intricate battery composition highlights the need for advanced recycling processes to recover the majority of valuable metal content.

Hydrometallurgical processes are the main alternative for recycling NiMH batteries, in which battery powders are generally leached in a mineral acid, such as HCl<sup>[13,16–23]</sup> (around 40% of the recent literature) or H<sub>2</sub>SO<sub>4</sub> (about 60%).<sup>[2,3,28–32,10,12,14,18,24–27]</sup>

[a] M. Zielinski, Dr. L. Cassayre, P. Destrac, Dr. B. Biscans  
Laboratoire de Génie Chimique  
Université de Toulouse, CNRS, INPT, UPS  
Toulouse (France)  
E-mail: beatrice.biscans@toulouse-inp.fr

[b] M. Zielinski, Dr. N. Coppey, Dr. G. Garin  
Société Nouvelle d'Affinage des Métaux (S.N.A.M.)  
Viviez (France)

To a minor extent, a few researchers have studied the use of  $\text{HNO}_3$ ,<sup>[13,29]</sup> carboxylic acids,<sup>[12,21]</sup> or ascorbic acid as leaching agents, but these have not been considered in this study. It is crucial to control the leaching step because the content of dissolved metals in solution will have a direct impact on subsequent recovery methods, such as precipitation or solvent extraction. Most of the literature on the leaching of spent NiMH batteries focuses on the impact of various operating parameters, such as type and concentration of acid, temperature, time, mixing speed, and addition of an oxidant. A nearly total dissolution of nickel and REEs is commonly sought-after, and thus, requires the use of aggressive leaching conditions: either high working temperatures (70–95 °C) or high acid concentrations (8–12 M). However, in view of more sustainable NiMH battery recycling processes, it is interesting to find milder leaching conditions. Although recent studies have been carried out in this regard,<sup>[13,21,23]</sup> it is still necessary to better understand the particle leaching mechanisms at stake.

Moreover, at the industrial scale, spent NiMH batteries undergo specific head-end steps before leaching, such as thermolysis, milling, and sieving. Indeed, spent battery packs are first collected and sorted according to their type. Then they are processed through a heat treatment under a controlled atmosphere (thermolysis) to remove volatile organic components and make the batteries electrically inert. The material is then milled and sieved to obtain a powder enriched in valuable elements, such as nickel and REEs. These processing steps impact on both the chemical and physical properties of the starting material, and might consequently influence the leaching process. However, apart from a few studies,<sup>[10,12,14,33]</sup> the initial material in most reports in the literature comes from manually dismantled batteries that have not gone through these pretreatment steps.

The aim of this work is, therefore, to provide a better understanding of the leaching behavior of nickel and REEs from industrial powders of spent NiMH batteries, the so-called black mass (BM) powder. The originality of this research lies in the fact that we have carried out in-depth particle characterization of a heterogeneous material with respect to that found at the industrial scale. The methodology applied for initial material characterization was then transferred to the analysis of solid leach residue, which was obtained from leaching experiments carried out in a 10 L pilot-scale reactor. Furthermore, to consider a more sustainable process at the industrial scale, we selected mild temperature (25 °C <  $T$  < 60 °C) and pH (3 < pH < 5.5) operating conditions for the leaching experiments, in two acid media (HCl and  $\text{H}_2\text{SO}_4$ ).

## Results

### BM powder characterization

An industrial sample of approximately 600 kg of mixed types of spent NiMH batteries was collected. The battery packs, which were composed of a mixture of anodes, cathodes, and casing materials, were processed at industrial facilities. They were dismantled, thermolyzed in an oven, crushed by knife

milling, and sieved at < 1 mm. The resulting powder, BM, was carefully characterized before being used as a starting material for the leaching study.

### Chemical composition and phase analysis

The average chemical composition of four samples of industrial BM powder from the same batch is provided in Table 1 (see the Experimental Section for all analytical details). The BM powder is mainly composed of 45.0 wt% Ni, approximately 15.9 wt% REEs (La, Ce, Nd, Pr), 13.1 wt% O, 5.4 wt% Co, and

**Table 1.** Average chemical composition [wt%] of the industrial BM sample powder.

Element	Chemical composition [wt%]
Al	0.85 ± 0.01
Cd	0.83 ± 0.05
Co	5.45 ± 0.23
Cu	0.51 ± 0.03
Fe	2.90 ± 0.32
K	2.17 ± 0.07
Li	0.13 ± 0.01
Mn	2.37 ± 0.14
Na	< detection limit
Zn	1.56 ± 0.19
Ni	44.98 ± 0.69
La	8.72 ± 0.22
Ce	5.02 ± 1.09
Nd	1.68 ± 0.05
Pr	0.45 ± 0.01
O	13.1 ± 0.1
C	2.83
total	93.65

2.4 wt% Mn. Although the contents of Co and Mn in the BM powder are significant and these metals have a noticeable economic value, herein we have chosen to report only results for the major elements Ni and REEs. The presence of K (2.2 wt%) is attributed to residual KOH electrolyte. Sodium is absent from the BM (below the detection limit), and traces of cadmium and lithium are due to cross contamination from other types of batteries during the manual battery-sorting step. Elemental carbon (2.8 wt%) most likely comes from the residue of organic components formed during heat treatment of the batteries. A total chemical composition of 93.65 wt% is obtained; the missing mass can be explained by the fact that additional elements such as Y or Sm have not been analyzed and that a small quantity of BM could not be dissolved prior to elemental analysis.

The powder X-ray diffractogram (Figure S1 in the Supporting Information) provides evidence of the presence of Ni, NiO,  $\text{CeO}_2$ , and graphite as major phases. Minor phases include  $\text{Co}_3\text{La}_2$  and  $\text{La}_7\text{Ni}_{16}$ ; other rare-earth-containing phases could not be identified due to the detection limit of the technique.

## Local elemental particle characterization

Although local electron probe microanalyses (EPMA) infer that both the morphology and associated chemical composition of the BM particles are very heterogeneous, our observations lead us to propose a classification into five main categories of particles.

P1-type particles observed and characterized by means of scanning electron microscopy energy-dispersive X-ray spectroscopy (SEM-EDX; not shown herein) consist of individual iron oxide and aluminum oxide particles, with a characteristic dimension of about 30  $\mu\text{m}$ , possibly originating from the outer casing of the battery.

As shown in Figure 1, zone 1, P2-type particles containing around 97 at% Ni were evidenced (Table 2). They come from the metallic nickel mesh of the cathode current collector and correspond to the nickel phase identified by means of powder XRD.

P3-type particles consist of circular porous particles, single or agglomerated, that contain, on average, 78.0 at% Ni, 5.3 at% Co, and 4.8 at% O (Figure 1, zone 2, and range of compositions in Table 2). Given their morphology, it can be stipulated that P3-type particles come from the active mass of the

cathode, which are originally spherical  $\text{Ni}(\text{OH})_2$  or  $\text{NiO}(\text{OH})$  particles, depending on the state of charge of the battery, although a higher oxygen content would be expected.

Particles rich in REEs have been categorized as either of P4 or P5 type. As shown in Figure 1, zone 3, P4-type particles exhibit a geometric shape with a dense and smooth external surface. EPMA point analyses on several P4 particles give molar ratios of  $(\text{Ni}, \text{Co}, \text{Mn}, \text{Al})/(\text{La}, \text{Ce}, \text{Nd}, \text{Pr})$  in the range of 1.9 and 4.6 (Table 2). The specific Ni/La molar ratio of 2.20 obtained for some P4-type particles is almost equivalent to that of the  $\text{La}_7\text{Ni}_{16}$  phase identified by means of powder XRD. On the other hand, P5-type particles shown in Figure 1, zone 4, exhibit a core-shell structure; the core is composed of 38.0 at% Ni, 34.9 at% O, and 4.1 at% La on average. The  $(\text{Ni}, \text{Co}, \text{Mn}, \text{Al})/(\text{La}, \text{Ce}, \text{Nd}, \text{Pr})$  molar ratios of P5-type particles are in the range of 3.8 and 4.9 (Table 2). The range of compositions found for P4- and P5-type particles can be attributed to the heterogeneity of the initial material; the sample is composed of different types of spent NiMH batteries.

A high-magnification cross section of a P5-type particle with a representative core-shell structure and corresponding EPMA line profile are shown in Figure 2. Around the core (the lighter part on the micrographs), the shell is composed of a dense, thin layer (Figure 2b) covered by a porous matrix. The EPMA line profile (Figure 2d) reveals that the dense layer of the shell (the two points at 1.8 and 3.5  $\mu\text{m}$ ) contains, on average, 1.35 times more Ni and Co than that in the core (points at <1.8 and >4.7  $\mu\text{m}$ ). As for the porous matrix (point at 3.0  $\mu\text{m}$ ), it has high contents of La, Ce, and O of 23.9, 8.1, and 20.1 at%, respectively, whereas the Ni and Co contents drop to 8.8 and 1.1 at%, respectively (Figure 2d).

The core-shell structure of P5-type particles is most likely linked to NiMH battery aging mechanisms. Indeed, the degradation of NiMH batteries is a complex process in which different mechanisms are at play, including corrosion of the hydrogen storage alloy. It is worth noting that the stability of the mischmetal alloy against corrosion can be impacted by the chemical composition of the alloy, among other parameters. According to the groups of Leblanc and Bäuerlein, changes in corrosion rates as a function of alloy composition are mainly due to differences in decrepitation tendencies.<sup>[34,35]</sup> Decrepitation, or particle pulverization, is caused by lattice expansion and contraction of the alloy during hydrogen absorption

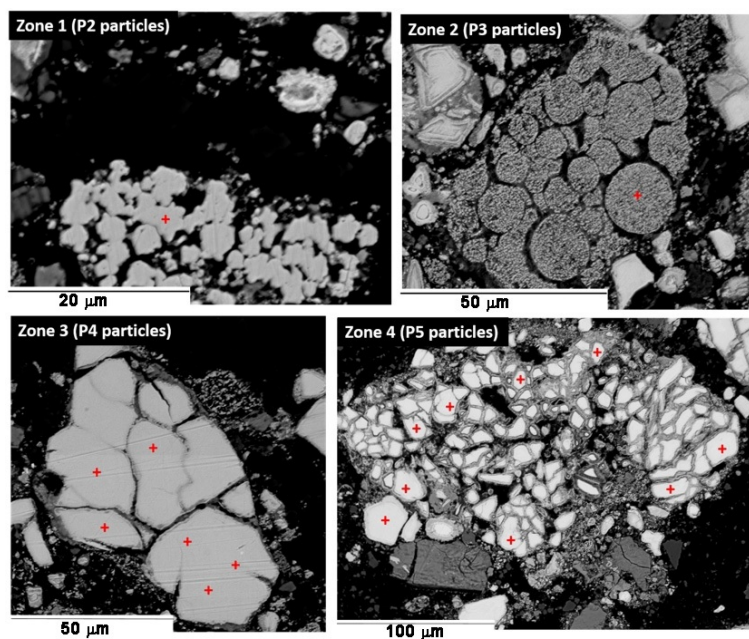


**Figure 1.** SEM backscattered electron (BSE) cross sections of representative BM particles: P2 type (zone 1), P3 type (zone 2), P4 type (zone 3), and P5 type (zone 4).

**Table 2.** EPMA WDS range of atomic contents of P2 type, P3 type, P4 type and P5 type BM particles [at%].

Particle type	Atomic content [%]											(Ni,Co,Mn,Al):(REEs)
	O	Al	K	Mn	Co	Ni	Pr	Nd	La	Ce	Total	
P2	1.2 1.4	0	0 0.1	0.1 0.2	0.3 0.9	97.4 97.7	0	0	0	0	100	
P3	2.0 8.1	0.2 0.4	0.2 1.4	0.1 0.4	2.9 7.3	62.0 93.6	0	0	0	0	92.0	
P4	9.5 33.0	1.1 3.0	0 0.2	3.7 4.3	6.2 8.7	42.1 43.6	0.3	1.4 2.4	6.0 19.8	3.2 8.2	99.9	1.9 4.6
P5	31.8 36.9	2.8 4.4	0 0.9	3.9 5.4	5.8 7.8	35.6 41.0	0.5 0.6	1.4 2.2	3.5 4.7	4.7 6.5	100	3.8 4.9

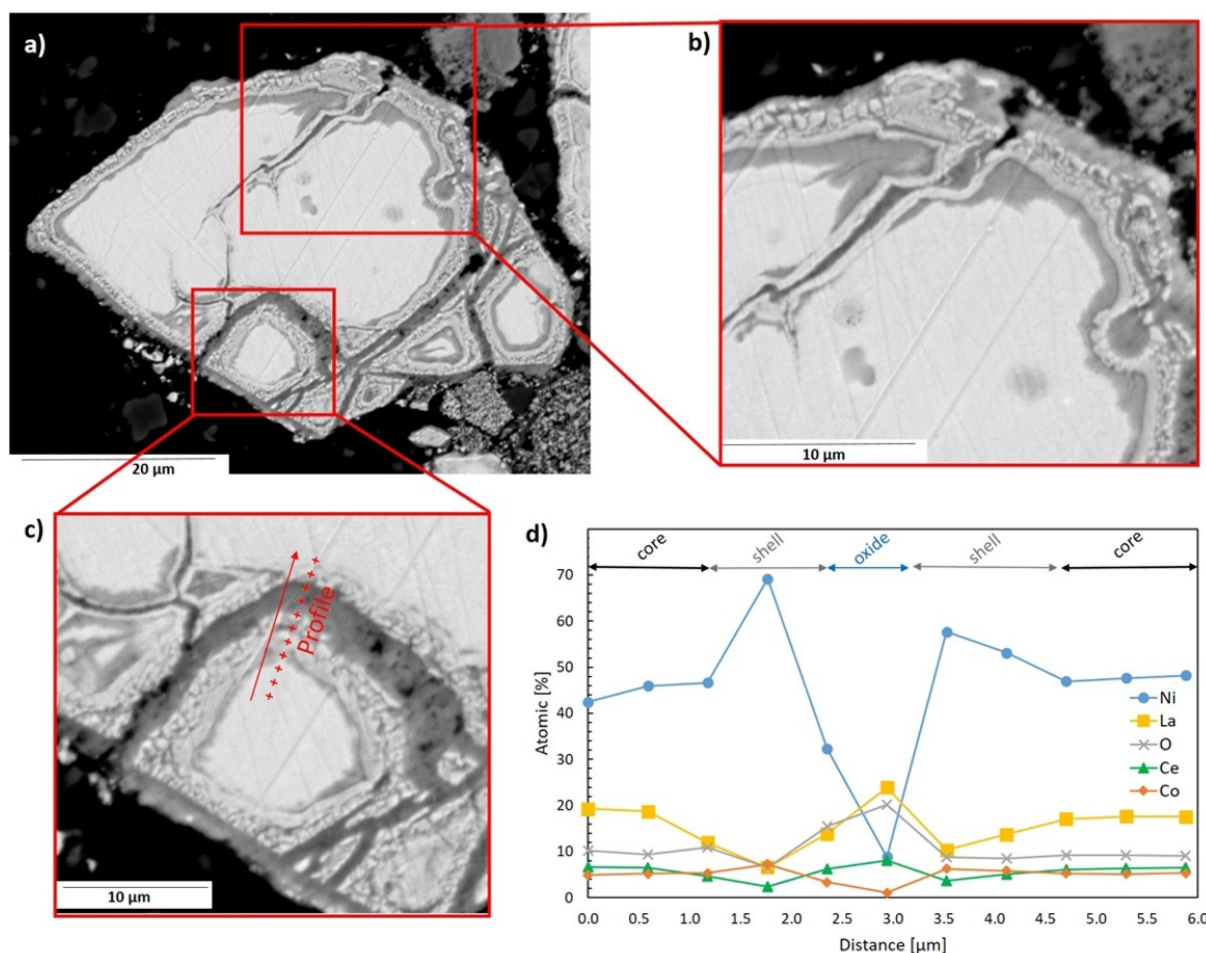


**Figure 2.** a) SEM BSE cross section of a P5 type BM particle with a core shell structure, b) first magnification of the core shell oxide structure, c) second magnification of the core shell oxide structure, and d) corresponding EPMA WDS line profile [at%].

and desorption. The discrete volume changes produce local mechanical stresses that lead to cracking of the alloy grains, the generation of smaller particles, and the development of a higher particle specific surface area.<sup>[34–36]</sup> Knowing that, from a thermodynamic point of view, the oxidation of less noble metals, such as La, Nd, Pr, and Ce, in KOH cannot be avoided,<sup>[36]</sup> the higher the particle specific surface area the greater the amount of corrosion scales. Therefore, there is a correlation between the decrepitation tendency of the mischmetal alloy and the corrosion of the particles. Consequently, alloy composition can be optimized to achieve low lattice expansions during hydrogen intercalation. For example, Chartouni et al. stated that cobalt substitution in the mischmetal alloy had a stabilizing effect by reducing the cracking tendency of the alloy.<sup>[37]</sup>

Several studies in the literature report that corrosion scales form at the surface of the particles in strong-alkali media, retarding hydrogen diffusion rates and leading to battery failure.<sup>[15, 21, 34–36, 38–40]</sup> Maurel et al. analyzed TEM cross sections of AB<sub>3</sub> mischmetal cycled in KOH electrolyte, and suggested the formation of three different corrosion layers due to solid-state diffusion: a metallic core different from that of the initial alloy, a continuous corrosion subscale up to 200 nm thick composed

of solid solutions of Ni and Co, and a surface layer of rare-earth hydroxide composed of 1.5 μm long needles embedded in the corrosion subscale.<sup>[36]</sup> Nickel and cobalt sublayers were also identified by the groups of Ikoma<sup>[38]</sup> and Bäuerlein,<sup>[35]</sup> and several other authors indicated that needle-shaped rare-earth hydroxides covered the surface of the alloy upon battery cycling in alkali media.<sup>[15, 34–36, 38]</sup>

Based on these consistent observations, we postulate that P4-type particles correspond to unused battery material (Figure 1, zone 3), whereas the core-shell structure of P5-type particles identified in the BM correspond to aged alloys (Figure 1, zone 4, and Figure 2). The nickel and cobalt sublayer identified in the literature corresponds to the dense layer of the shell of P5-type particles shown in Figure 2. The porous matrix rich in La, Ce, and O observed around P5-type particles (Figure 2c) may thus originate from the disintegration of the needle-like rare-earth hydroxide surface layer. Moreover, based on the observation of various cross sections of the BM samples, there are proportionally many more P5-type particles than that of P4-type particles, which is consistent with the fact that most batteries are collected if fully spent.

On top of structural changes caused by corrosion of the anode during battery cycling, the thermolysis step is very likely

to induce structural and chemical evolutions of the mischmetal alloy. However, the impact of thermolysis linked to battery re-processing is related to more recent concerns than those of battery aging, and thus, is not yet documented in the literature. Nevertheless, based on a thermodynamic study of the La–Ni–O ternary system by Zinkevich and Aldinger, it is very likely that thermolysis leads to the formation of the stable  $\text{La}_2\text{NiO}_4$  spinel.<sup>[41]</sup> Indeed, this lanthanum nickelate is stable over a large range of oxygen partial pressure (typically  $10^{-8}$  atm  $< P_{\text{O}_2} < 10^{-1}$  atm), covering thermolysis operating conditions. For Ni/(Ni, La) molar ratios greater than 0.5, the phase diagram indicates that the spinel phase is the first phase that forms from the oxidation of a Ni–La alloy, followed by oxidation of nickel into NiO. The results of Zinkevich et al. could explain both the high oxygen content observed at the core of P5-type particles (Table 2 and Figure 2d) and the NiO phase detected by means of powder XRD.<sup>[41]</sup>

Altogether, the EPMA characterization is coherent with the initial constitution of NiMH batteries, and particles from the anode and cathode active mass, as well as current collectors have been identified and quantified. Thanks to this local particle identification approach, it is thus possible to follow the leaching progress by comparing the particles identified in the initial BM powder with those in the solid leach residue over time.

### Thermodynamic-based choice of pH for leaching experiments in HCl media

The choice of pH for leaching experiments in HCl was guided by thermodynamic calculations. Considering the complex phase composition of the initial BM powder, the system was restricted to the system Ni–La–H<sub>2</sub>O–HCl because Ni and La are the major elements in the BM. The Eh–pH diagrams calculated at 40 °C for La and Ni are presented in Figure 3a and b, together with the list of aqueous species and solid phases taken into account in Figure 3c. Calculation details are provided in the Experimental Section.

As observed in Figure 3a, La is not stable in its metallic form in aqueous media. At pH  $\leq 6.8$  and 40 °C (or pH  $\leq 7.1$  at 25 °C; pH  $\leq 6.3$  at 60 °C), La is fully dissolved, mainly as  $\text{LaCl}^{2+}$ . At higher pH, its stable form is the solid hydroxide  $\text{La}(\text{OH})_3$ .

As for Ni (Figure 3b), a lower pH is required to ensure its full dissolution (pH  $\leq 4.2$  at 40 °C) and  $\text{Ni}^{2+}$  is the aqueous dominant species for all temperatures; the complex  $\text{NiCl}^+$  is present to a minor degree. Above pH 4.2 at 40 °C, metallic nickel is stable and is not oxidized by  $\text{H}^+$  ions. Nickel(III) is soluble up to pH 6, and forms the solid hydroxide  $\text{Ni}(\text{OH})_2$  at higher pH.

Notably, solids composed of both Ni and La elements ( $\text{LaNi}_5$  and  $\text{La}_2\text{NiO}_4$ ) do not appear on these diagrams, which means that the main mixed phases of the battery are not stable under leaching conditions.

These preliminary calculations indicate that, for a solid/liquid (S/L) ratio of 15 wt%, both nickel and lanthanum elements should be soluble at pH 4 and below, regardless of their initial redox state. At  $4 < \text{pH} < 6$ , La and  $\text{Ni}^{\text{II}}$  are soluble, but metallic Ni is stable. At  $6 < \text{pH} < 6.8$ , La is stable in the aqueous phase, whereas all redox states of Ni are involved in solid phases. Above pH 6.8, no dissolution of these two major elements in the BM should occur. These calculations imply a strong influence of pH on the leaching behavior of the BM, and suggest that tuning the pH value might allow the selective dissolution of La. Therefore, the influence of pH on leaching of the BM was studied over the pH range of 3 to 5.5, and pH 3 was used as a point of comparison for studying the influence of the type of acid (HCl or H<sub>2</sub>SO<sub>4</sub>) on the leaching yields and rates with respect to temperature.

### Leaching experiment results

As detailed in the Experimental Section, BM leaching experiments were carried out in a 10 L pilot reactor. The results are presented in the following sections, starting with the influence of temperature, then pH, and finally the nature of the acid.

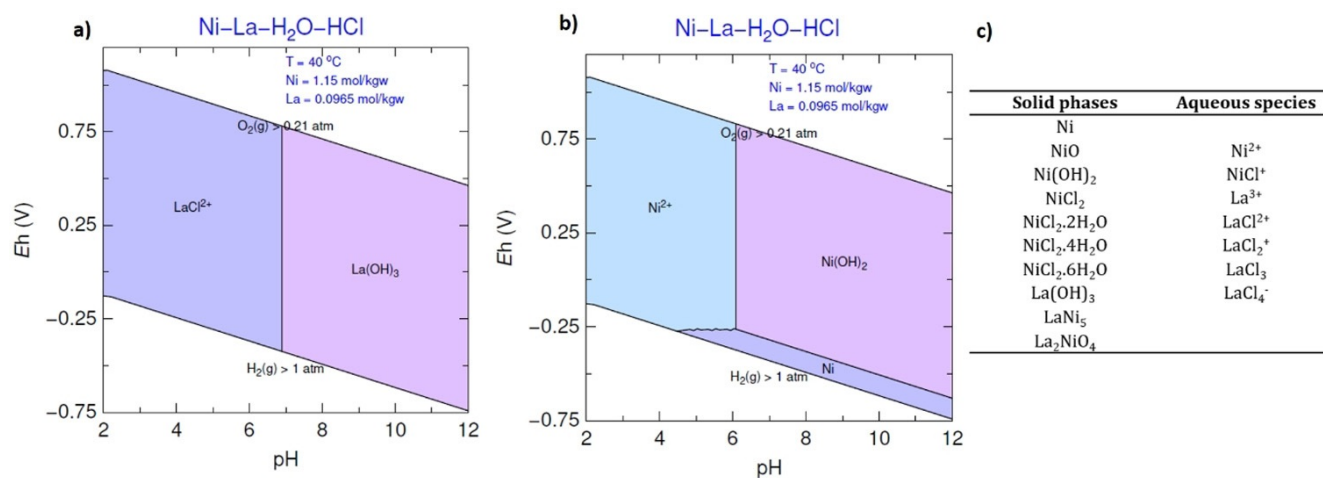


**Figure 3.** Calculated Eh–pH diagram for a) La and b) Ni, in the quaternary system Ni–La–H<sub>2</sub>O–HCl at 40 °C, with  $[\text{La}] = 0.0965$  mol kgw<sup>−1</sup> (kilograms of water) and  $[\text{Ni}] = 1.15$  mol kgw<sup>−1</sup> (S/L ratio of 15 wt%). c) List of the solid phases and aqueous species considered for thermodynamic calculations.

## Influence of temperature

The influence of temperature on the leaching yields of La and Ni in HCl at pH 3 is shown in Figure 4a; similar behavior to that of La is obtained for Ce, Nd, and Pr. The experiment at 40 °C was repeated twice and demonstrated good repeatability of the leaching yields and total acid consumption: a difference of less than 3.1 and 5.4% for the leaching yields of Ni and La, respectively, and a relative difference of 1.2% for the acid consumption were obtained between both experiments after 6 h of leaching.

Regardless of the temperature, La (and other REEs) leaching yields increase gradually and converge to complete dissolution (Figure 4a) after 22 h. As for Ni, a leaching yield of 58% is reached after 22 h at 60 °C, and the yield decreases with temperature. The leaching in HCl at pH 3 is thus partially selective: a maximal La/Ni selectivity ratio of about 6.5 is obtained for all three temperatures, and the time at which this maximum is

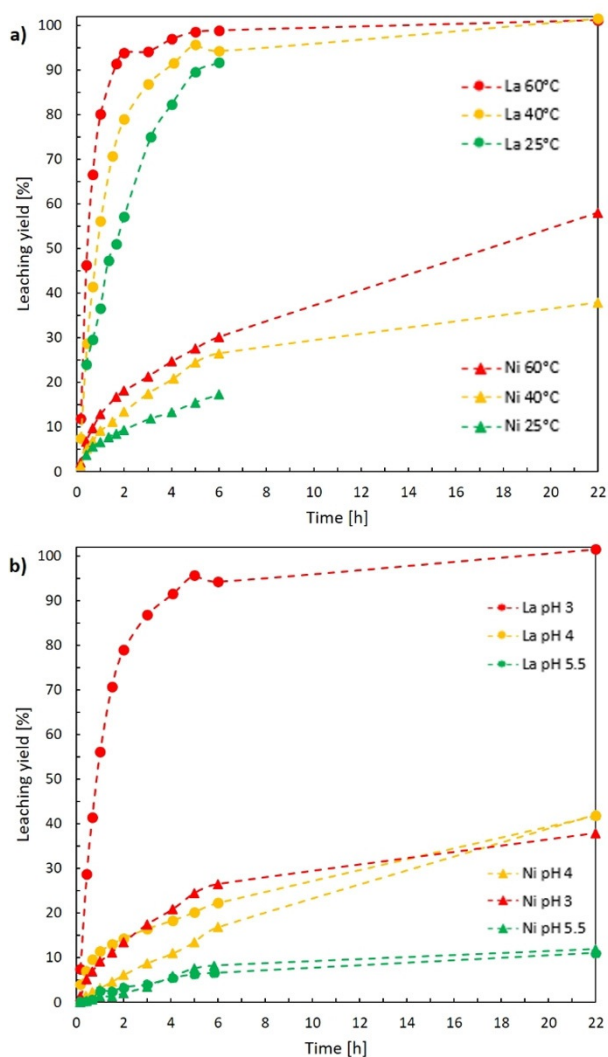


**Figure 4.** a) Influence of the temperature in HCl at pH 3 on the leaching yields of La (circles) and Ni (triangles). b) Influence of the pH in HCl at 40 °C on the leaching yields of La (circles) and Ni (triangles).

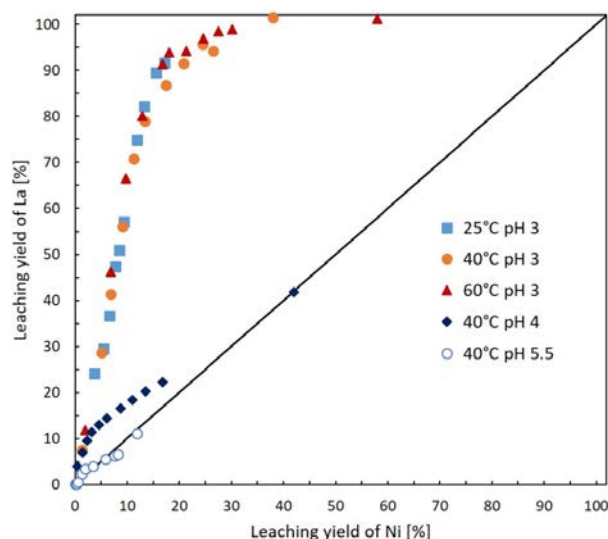


**Figure 5.** Leaching yield of La [%] expressed with respect to the leaching yield of Ni [%] for experiments carried out in HCl at various pH and temperature (the black line corresponds to a congruent dissolution of La and Ni).

reached greatly reduces with temperature (after 3 h at 25 °C, 1.5 h at 40 °C, and 36 min at 60 °C). The evolution of the leaching yield of La with respect to that of Ni at pH 3 is plotted in Figure 5. Considering that, thermodynamically, both La and Ni are soluble in HCl–H<sub>2</sub>O under these conditions (Figure 3), the fact that all experimental points are located above the bisecting line shows that the leaching kinetics of REEs are faster than that of Ni. Moreover, all experimental points at pH 3 overlap, which demonstrates a similar leaching mechanism, regardless of temperature. At pH 3 in HCl, the temperature only enhances the overall reaction kinetics and an increase of 35 °C (from 25 to 60 °C) decreases the leaching duration by a factor of about 3.

Evolution of the chemical composition of the solid leach residues after mineralization (Table S1 in the Supporting Information) indicates an overall enrichment in Ni and a depletion in REEs, with respect to the initial BM powder, which is in agreement with the ICP-OES analyses of the pregnant leach solution (PLS). Powder XRD analysis of all solid leach residues shows that the major phases present in the initial BM powder are still present even after 22 h of leaching at 60 °C, namely, Ni, NiO, and graphite (Figure S2 in the Supporting Information).

It is interesting to identify P2- and P5-type particles in the solid leach residue, knowing that they are the ones which contain the highest contents of Ni and REEs. According to SEM and EPMA characterizations, many P2-type particles (pure Ni) are still present (Figure 6, zone 5) in the solid leach residue after 22 h of leaching at 60 °C.

A striking observation is that the core-shell structures of P5-type particles identified in the initial BM powder are still clearly apparent in all solid leach residues. After 1 h of reaction in HCl at pH 3 and 60 °C, that is, shortly after the maximum La/Ni selectivity ratio is reached, the composition and morphology of particles shown in Figure 6, zones 1 and 2, illustrate the leaching mechanism. According to the EPMA wavelength-dispersive

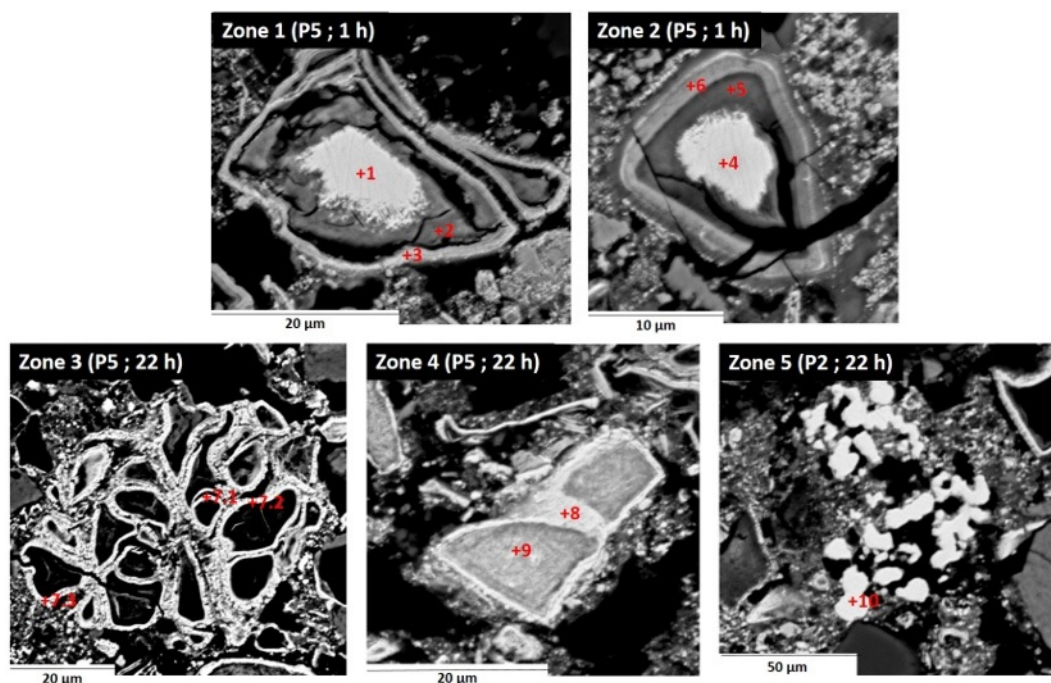


**Figure 6.** SEM BSE cross sections of particles in the solid leach residue obtained in HCl at pH 3 and 60 °C, after 1 h of leaching (zones 1 and 2) and after 22 h of leaching (zones 3–5).

Region		Composition [at%]										Total
		O	Al	K	Mn	Co	Ni	Pr	Nd	La	Ce	
zone 1	1	9.2	1.6	0.0	3.6	9.3	44.1	1.5	5.2	10.3	12.7	97.4
	2	15.1	0.2	0.3	0.1	6.5	42.6	0.2	0.4	0.9	1.2	67.6
	3	4.2	0.0	0.1	0.2	14.0	75.6	0.2	0.4	1.6	1.0	97.5
	4	9.5	1.7	0.0	4.6	8.5	42.1	1.2	4.2	10.7	13.8	96.5
zone 2	5	16.0	0.0	0.2	0.0	6.6	41.0	0.1	0.1	0.1	0.1	64.2
	6	13.6	0.2	0.1	0.0	8.4	47.6	0.0	0.2	0.3	0.6	70.9
zone 3 <sup>[a]</sup>	7	26.8	1.0	0.0	0.1	8.9	62.1	0.0	0.1	0.2	0.2	101.5
	8	24.5	0.9	0.0	0.1	9.6	63.2	0.0	0.1	1.1	0.5	100
zone 4	9	40.4	0.8	0.1	0.1	7.2	50.0	0.0	0.1	0.9	0.5	100
	10	1.2	0.0	0.0	0.0	0.31	98.0	0.0	0.0	0.0	0.0	100

[a] Average at% at points 7.1, 7.2, and 7.3.

spectroscopy (WDS) point analyses (Table 3, zone 1), the core of the dissolving particle contains about 30 at% REEs, whereas the intermediate layer and shell contain 2.6 and 3.3 at% REEs, respectively. Moreover, compared to the core, the shell of the particle contains high amounts of Ni (75.6 at%) and is enriched in Co (14.0 at%; Figure 6, zone 1, and Table 3), which is close to the composition of the shell of P5-type particles in the initial BM powder (Table 2). An EPMA concentration profile measured across a larger particle (Figure 7) provides evidence that the shell contains between 70 and 90 at% Ni and 10 and 20 at% REEs. Overall, these observations show that REEs dissolve preferentially to nickel from the core of the particles, and that nickel contained in the dense outer shell does not dissolve.

Such a leaching mechanism is also evidenced in the cross sections of the solid leach residue after 22 h of dissolution in

HCl at pH 3 and 60 °C, where the structure of the remaining particles is either a porous shell with a hollow core (Figure 6, zone 3) or a core-shell structure with an undissolved core (Figure 6, zone 4). The shells of the hollow particles appear to be porous, and thus, allow REEs to dissolve. According to EPMA analyses (Table 3), the shells of these hollow particles are composed of approximately 62.1 at% Ni, 8.9 at% Co, and less than 0.5 at% REEs. The shells of the particles with an undissolved core have almost the same composition (Table 3), while their core contains 50.0 at% Ni, 7.2 at% Co, 40.4 at% O, and less than 1.5 at% REEs. These results indicate that the shells and nickel-rich cores of the remaining particles, originally from the spent active mass of the anode, have very slow leaching kinetics in HCl at pH 3, similarly to the metallic nickel mesh of the cathode.

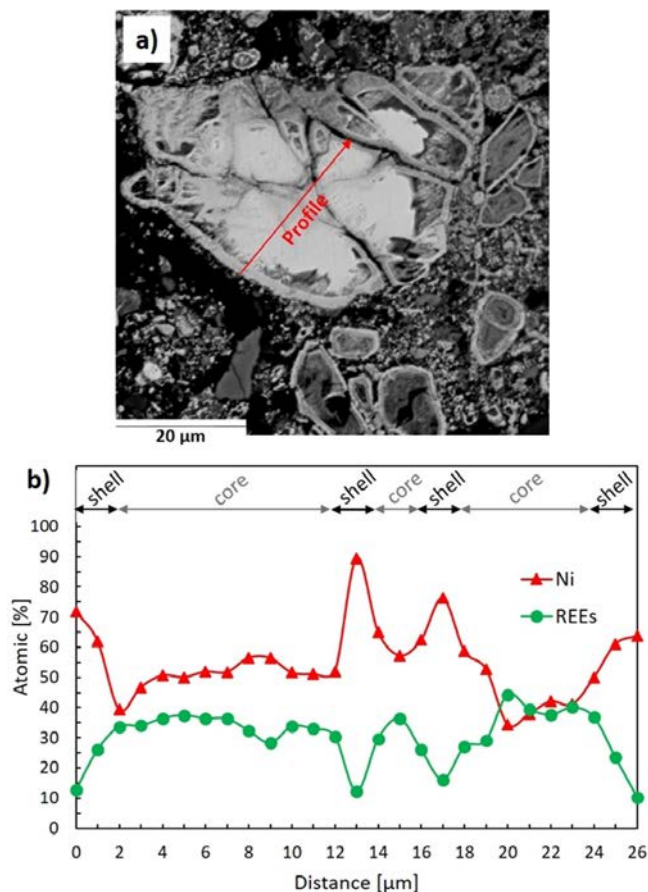


**Figure 7.** a) SEM BSE cross section of a particle after 1 h of leaching in HCl at pH 3 and 60 °C. b) Corresponding EPMA WDS concentration profile obtained across the particle [at%].

### Influence of pH

The influence of pH on the evolution of the leaching yields of REEs and Ni in HCl at 40 °C is shown in Figure 4 b. After 22 h of leaching at 40 °C, the recovery yield of Ni decreases from 37.9% at pH 3 to only 11.9% at pH 5.5. Meanwhile, the La recovery yield drops from 100% at pH 3 to 11.1% at pH 5.5. Similar leaching behavior as La is obtained for Ce, Nd, and Pr at pH 3 and 4, whereas at pH 5.5 Ce, Nd, and Pr have lower leaching yields than that of La of 8.0, 5.2, and 4.4%, respectively, after 22 h of leaching at 40 °C. As observed in Figure 5, at pH 5.5 and 40 °C, if the leaching yield of La is plotted against that of Ni, the experimental points are almost aligned with the bisecting line. According to our thermodynamic calculations under these conditions, La and Ni<sup>II</sup> (from the phases La<sub>2</sub>NiO<sub>4</sub> and NiO) are soluble, whereas metallic Ni should remain solid (Figure 3). Therefore, we hypothesized that the low leaching yield obtained for nickel shows that Ni<sup>II</sup> has slow leaching kinetics at pH 5.5, which consequently hinders the dissolution rate of REEs through the creation of a thicker diffusion layer than that at pH 3.

XRD analysis of the solid leach residues obtained at pH 4 and 5.5 at 40 °C in HCl after 22 h of leaching (Figure S3 in the Supporting Information) reveals that they are composed of the

same major phases as those present in the initial BM powder, namely, Ni, NiO, CeO<sub>2</sub>, and graphite.

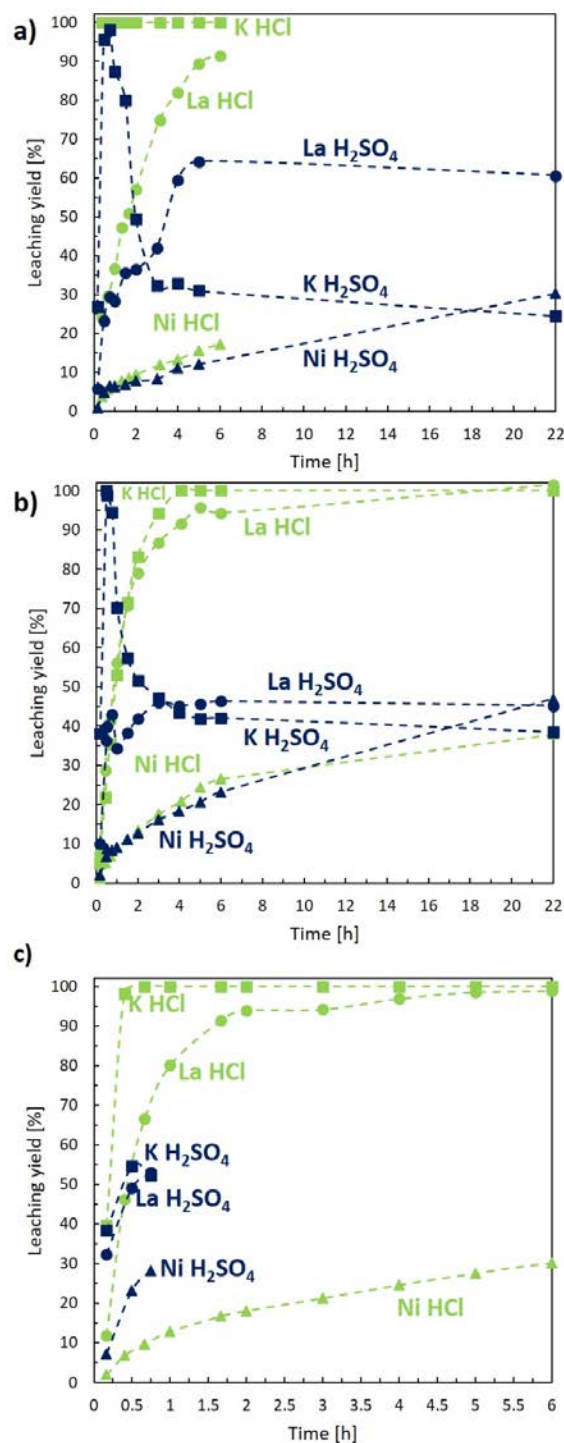


**Figure 8.** Evolution of the leaching yields of K (squares), La (circles), and Ni (triangles) in HCl (blue) and H<sub>2</sub>SO<sub>4</sub> (green) at pH 3 and at a) 25, b) 40, and c) 60 °C.

## Influence of the type of acid

The influence of the leaching agent (HCl or H<sub>2</sub>SO<sub>4</sub>) on the dissolution of REEs, Ni, and K has been studied at pH 3 for temperatures ranging from 25 to 60 °C. Under these conditions, both acids are completely dissociated ( $pK_a(\text{HCl}/\text{Cl}^-) = 6.3$ ,  $pK_a(\text{H}_2\text{SO}_4/\text{HSO}_4^-) = 3.0$ , and  $pK_a(\text{H}_2\text{SO}_4/\text{SO}_4^{2-}) = 2.0$  at 25 °C).

Again, all REEs (La, Ce, Nd, and Pr) exhibit similar leaching behavior. Thus, only La is considered in the following discussion. As illustrated in Figure 8a and b, at pH 3 and 25 or 40 °C, the leaching yield of Ni follows similar trends in H<sub>2</sub>SO<sub>4</sub> and in HCl: yields of only 12.1 and 20.5 % are obtained after 5 h, respectively. At 60 °C, however, nickel is more reactive in H<sub>2</sub>SO<sub>4</sub> than that in HCl (Figure 8c): the same quantity is leached in 45 min in H<sub>2</sub>SO<sub>4</sub> than that after 5 h in HCl. It is worth noting that, for the experiment carried out in H<sub>2</sub>SO<sub>4</sub> at pH 3 and 60 °C, much greater acid consumption and gas production were observed than that at 25 or 40 °C. The increase in gas production, which is attributed to H<sub>2(g)</sub> generation, indicates more reactive dissolution of metallic nickel with increased temperature. The large difference in leaching behavior between 40 and 60 °C was also observed by Hosseini et al., who studied the leaching kinetics of NiO and NiFe<sub>2</sub>O<sub>4</sub> from nickel tailings in 4 M H<sub>2</sub>SO<sub>4</sub> at temperatures ranging from 25 to 80 °C.<sup>[42]</sup> They measured an abrupt increase in the leaching rate of nickel at 60 °C after 1 h of leaching, and attributed it to the fact that below 40 °C only simple oxides dissolved, whereas spinel phases only started to dissolve after 1 h at 60 °C, and the reaction kinetics were then controlled by chemical reaction, rather than by diffusion.<sup>[42]</sup>

The data compiled in Figure 8 indicate that, for all temperatures, potassium precipitates in H<sub>2</sub>SO<sub>4</sub> media shortly after all BM powder has been added because the curve of the leaching yield has a negative slope after approximately 24 min. On the other hand, potassium is completely solubilized in HCl at pH 3 at any temperature. It is thus likely that La and other REEs co-precipitate with K because their recovery rates are first equivalent to those obtained in HCl (for  $t < 24$  min) and then lower as K starts to precipitate (Figure 8). At 25 °C, potassium precipitation stops after 3 h because the leaching yield remains constant at 30%, which is equivalent to 0.024 mol L<sup>-1</sup> of K (Figure 8a). After 3 h, a sharp increase in the La leaching yield is observed (Figure 8a) and reaches a final yield of about 61 % after 22 h. At 40 °C, the precipitation of both K and La stops after 3 h, leading to leaching yields of 47.1 (or 0.034 mol L<sup>-1</sup> of K) and 46.0 % (or 0.039 mol L<sup>-1</sup> of La), respectively, which indicates that a solubility limit is reached (Figure 8b).

Mineralization of the solid leach residues obtained after leaching in H<sub>2</sub>SO<sub>4</sub> at pH 3 indicates an increasing potassium content with time, which is coherent with the results of PLS analysis. No traces of sodium were detected.

The powder XRD spectra of the leach residues obtained after 30 min of leaching in H<sub>2</sub>SO<sub>4</sub> at pH 3 and 25 or 40 °C are almost equivalent to that of the initial BM powder, and no ad-

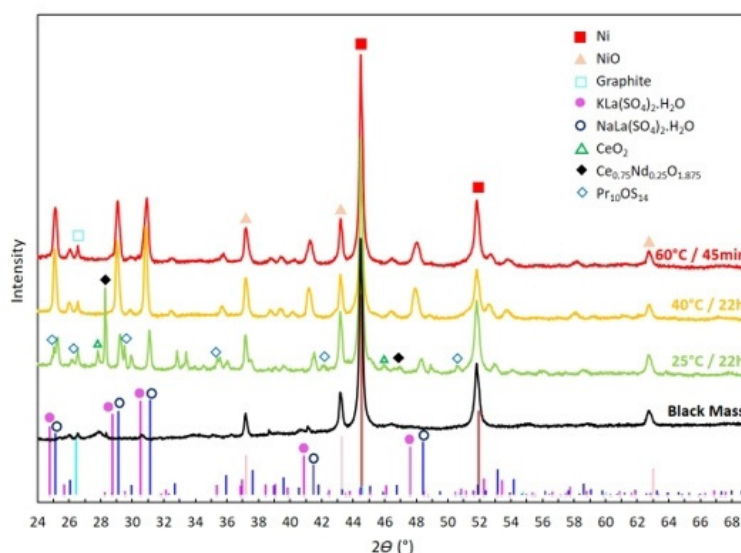


**Figure 9.** Powder XRD spectra of the initial BM sample (black) and the solid leach residues after dissolution in H<sub>2</sub>SO<sub>4</sub> at pH 3 and 25 °C for 22 h (green), at pH 3 and 40 °C for 22 h (yellow), and at pH 3 and 60 °C for 45 min (red).

ditional diffraction peaks are observed (Figure S4 in the Supporting Information). This confirms the results of leaching yield analysis, which show that potassium precipitation does not start until all BM has been added, that is, after 24 min (Figure 8). As observed in Figure 9, the major phases of Ni, NiO, and graphite are still present, even after 22 h of leaching in H<sub>2</sub>SO<sub>4</sub> for temperatures up to 60 °C. It is worth noting that the residue obtained after 22 h of leaching in H<sub>2</sub>SO<sub>4</sub> at pH 3 and 25 °C contains minor phases of Ce<sub>0.75</sub>Nd<sub>0.25</sub>O<sub>1.875</sub> and Pr<sub>10</sub>OS<sub>14</sub>, which are absent at 40 °C (Figure 9). This shows that, in H<sub>2</sub>SO<sub>4</sub>, the precipitation behavior changes between 25 and 40 °C.

Furthermore, for all solid leach residues shown in Figure 9, a pristine phase appears that could be ascribed either to NaLa(SO<sub>4</sub>)<sub>2</sub>·H<sub>2</sub>O or KLa(SO<sub>4</sub>)<sub>2</sub>·H<sub>2</sub>O. Because the BM powder does not contain Na and demineralized water is used for the experiments, we conclude that the peaks correspond to the phase KLa(SO<sub>4</sub>)<sub>2</sub>·H<sub>2</sub>O. Even if the XRD spectrum is not a perfect match because all peaks are slightly shifted to the right, with respect to the reference, this could be due to a mixed crystal composition. Indeed, several other lanthanide–potassium double sulfates (K<sub>3</sub>M(SO<sub>4</sub>)<sub>3</sub>, K<sub>6</sub>M<sub>4</sub>(SO<sub>4</sub>)<sub>9</sub>, K<sub>7</sub>M<sub>3</sub>(SO<sub>4</sub>)<sub>8</sub>, K<sub>5</sub>M(SO<sub>4</sub>)<sub>4</sub>, and K<sub>6+3n</sub>M<sub>4-n</sub>(SO<sub>4</sub>)<sub>9</sub>; M = La, Ce, Nd, or Pr) are reported in the literature.<sup>[14,43,44]</sup> Porvali et al. studied the precipitation of REEs from strong sulfuric acid NiMH battery waste leachate by the addition of Na<sub>2</sub>SO<sub>4</sub> and also observed a precipitate of mixed crystal composition with a structure close to that of the lanthanide–alkali double sulfate.<sup>[14]</sup>

SEM observations of cross sections of the solid residue obtained after 22 h of leaching in H<sub>2</sub>SO<sub>4</sub> at pH 3 and 40 °C, and corresponding EPMA point analyses, are compiled in Figure S5 and Table S2 in the Supporting Information. Particles with core–shell structures and compositions similar to those obtained in HCl are detected (Figure S5 in the Supporting Infor-

mation, zones 1–3). As illustrated in Figure S5 in the Supporting Information, many precipitates were found around the undissolved particles (points 5–10) and contained, on average, 65.9 at% O, 12.7 at% S, 8.5 at% REEs, 8.3 at% Ni, 3.4 at% K, and 0.7 at% Co (Table S2 in the Supporting Information). These local chemical analyses confirm the conclusions drawn from XRD analysis that REEs and K have coprecipitated. They also provide evidence of the coprecipitation of nickel and cobalt, probably in the form of double Tutton's salts, such as  $K_2Ni(SO_4)_2 \cdot 6H_2O$ ,  $K_2Co(SO_4)_2 \cdot 6H_2O$ , or  $K_2Ni_xCo_{1-x}(SO_4)_2 \cdot 6H_2O$ .<sup>[45–47]</sup> The precipitation of nickel could at least partially explain the slow increase in aqueous nickel concentration measured in  $H_2SO_4$  at pH 3 at 40 °C. Although it is not possible to determine accurately the precipitate composition due to its complexity, it is assumed that the precipitates consist of a mixture of potassium–lanthanide double sulfates and  $K_2Ni_xCo_{1-x}(SO_4)_2 \cdot 6H_2O$ .

## Discussion

The BM leaching mechanisms can be discussed thanks to a combination of all of our results (initial BM analyses, equilibrium calculations, evolution of the elemental concentrations in the PLS, and solid leach residue characterization by means of XRD, SEM, and EPMA). Whether in HCl or  $H_2SO_4$ , metallic Ni, which is identified as such in Figure 1, zone 1, and originating from the cathode current collector, dissolves according to Equation (1). Gas generation was also observed during the experiments.



However, despite favorable thermodynamics, according to the  $E_h$ –pH diagram at pH 3 (Figure 3b), a large part of nickel in its metal form remains in the solid leach residue, as indicated in the X-ray diffractograms and by means of EPMA-WDS analyses (Figure 6, zone 5, and Table 3). Similar observations were reported by the groups of Larsson<sup>[13]</sup> and Petranikova,<sup>[23]</sup> who studied separately the leaching of anodes and cathodes from NiMH batteries in HCl media. These authors postulated that hydrogen produced during the acid attack of nickel metal [Eq. (1)] desorbed slowly from nickel surfaces. Based on electronic orbital considerations, Santos et al. also concluded that the adsorbed hydrogen intermediate species,  $H_{ad}$ , implied in the redox reaction (e.g.,  $H_{ad} + H_{ad} = H_{2(g)}$  or  $H^+ + H_{ad} + e^- = H_{2(g)}$ ) significantly slowed down the dissolution of metallic nickel in HCl media.<sup>[48]</sup> For  $H_2SO_4$  media, a possible explanation for hindered nickel leaching could be the formation of a passivation layer on the Ni surface in the form of NiO or NiOOH, as reported by authors who have studied the anodic passivation of bulk Ni in  $H_2SO_4$  media.<sup>[49–52]</sup>

Similarly, nickel contained in the Ni/Co porous shell of P5-type particles and the Ni/Co/O core of some P5-type particles does not dissolve or has very slow leaching kinetics, which contributes to the selective leaching of REE relative to that of Ni. Indeed, in both acids, REE-containing particles (type P5), the core of which is mainly composed of lanthanum nickelates  $La_2NiO_4$ , exhibit selective leaching behavior, as evidenced by

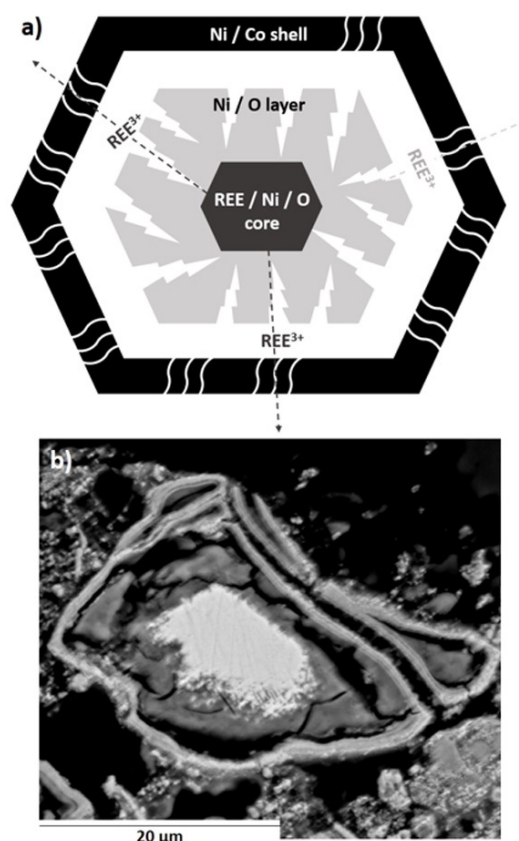


**Figure 10.** a) Schematic illustration of the proposed leaching mechanism of P5 type particles identified in Figure 2 in the initial BM sample powder, and b) the corresponding SEM BSE micrograph.

EPMA profiles such as that presented in Figure 7. The leaching rate of nickel is slower than that of REEs, resulting progressively in a hollow structure, as illustrated in Figure 10. It is suggested that dissolution of REEs [Eq. (2)] and their diffusion through the porous Ni/Co shell results in a shrunken core rich in REEs, whereas an intermediate layer depleted of REEs, but rich in Ni and O, remains and dissolves more slowly (Figure 10).



In HCl media, according to speciation obtained from thermodynamic calculations and consistent with experimental results, aqueous La forms soluble chloride compounds, such as  $LaCl^{2+}$  [Eq. (3)], whereas nickel dissolves mainly as  $Ni^{2+}$  and, to a lesser extent,  $NiCl^+$  [Eq. (4)]. As a consequence, the leached elements remain in the aqueous phase.

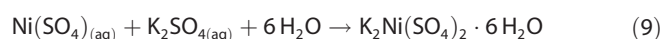
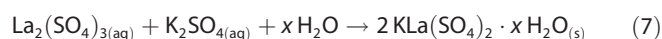


On the contrary, in  $H_2SO_4$  media, leached REEs precipitate in the form of sulfates,  $REE_2(SO_4)_3$ ; this behavior has also been reported elsewhere.<sup>[24,53,54]</sup> Furthermore, Zelikman et al. explain that lanthanide sulfates tend to form lanthanide–alkali double

salts in the presence of  $K_2SO_4$  or  $Na_2SO_4$ , according to Equation (5), in which  $M=K$  or  $Na$  and  $REE=La, Ce, Nd, \text{ or } Pr$ .<sup>[53]</sup>



Lokshin et al. measured the solubilities of double alkali-metal ( $Na, K$ )–rare-earth ( $La, Ce$ ) sulfates in solutions in sulfuric acid at 20 °C. For instance, at 20 °C and low  $H_2SO_4$  concentrations, the solubility of  $KLa(SO_4)_2 \cdot H_2O$  and  $KCe(SO_4)_2 \cdot H_2O$  is  $0.015 \text{ mol L}^{-1}$ , which is close to the potassium concentration of  $0.024 \text{ mol L}^{-1}$  measured at 25 °C after 3 h, which is the point at which potassium precipitation stops (Figure 8a).<sup>[53]</sup> Thus, in  $H_2SO_4$  media, part of the lanthanide ions form aqueous sulfate species [Eq. (6)], whereas others precipitate with  $K$  to form lanthanide–alkali metal double sulfates [Eq. (7)]. The main stable nickel species in  $H_2SO_4$  media is  $NiSO_{4(aq)}$  [Eq. (8)], but, as evidenced by our local characterization (Figure S5 and Table S2 in the Supporting Information), part of the nickel precipitates with  $K$ , according to Equation (9).



## Conclusions

An industrial sample of spent NiMH battery powder, which was obtained by the thermomechanical treatment of a batch of 600 kg, was characterized for chemical and structural properties. Chemical analysis revealed that the sample powder was mainly composed of 45 wt%  $Ni$ , 15 wt% REEs, and 13 wt%  $O$ , whereas XRD analysis demonstrated that the major crystalline phases consisted of  $Ni$  and  $NiO$ . A novel result was the quantitative EPMA-WDS analyses of cross sections of the powders, which helped to provide an overall description that was consistent with the initial battery constitution. Indeed, particles containing 97.4 at%  $Ni$  corresponded to the metallic nickel mesh of the cathode current collector and porous spherical particles rich in  $Ni$  and  $Co$  came from the cathode active mass. An interesting result was the identification of mischmetal particles with core–shell structures: at the core, the  $(Ni, Co, Mn, Al)/(La, Ce, Nd, Pr)$  molar ratio was 4.5, whereas the dense shell layer contained 1.35 times more  $Ni$  and  $Co$  than that in the core. Moreover, an oxide layer rich in REEs surrounded this dense shell. We attributed such particle morphology to NiMH battery aging mechanisms after cycling in  $KOH$  electrolyte, in which corrosion subscales concentrated in  $Ni$  and  $Co$  and REE hydroxide structures were known to form around the mischmetal particles.

In view of a sustainable recycling process, a parametric study was carried out in a 10 L pilot-scale reactor to assess the influence of pH (3–5.5), temperature (25–60 °C), and type of

acid ( $HCl$  or  $H_2SO_4$ ) on the leaching mechanisms of  $Ni$  and REEs contained in the industrial battery powders.

Partial selectivity was evidenced in  $HCl$  at pH 3 for all temperatures. For instance, at 25 °C, 91.6% of  $La$  and 17.2% of  $Ni$  leached after 6 h, leading to an aqueous  $La/Ni$  molar ratio of 5.31. In  $H_2SO_4$  media, a similar selective dissolution occurred at 25 and 40 °C, whereas nickel dissolution was enhanced at 60 °C. However, potassium present in the initial battery powder (about 2 wt%  $K$ ) led to the in situ precipitation of REEs in the form of lanthanide–potassium double sulfates, as well as the precipitation of nickel and cobalt double salts; thus reducing their overall dissolution yields.

One of the reasons for the selective dissolution of REEs, with respect to  $Ni$ , was due to the kinetic inhibition of nickel metal leaching, in both  $HCl$  and  $H_2SO_4$ , as already reported in several studies. In the present work, thanks to local EPMA analyses of the solid leach residues, we also showed that specific leaching mechanism occurred in the core–shell mischmetal particles, in both acid media. The  $Ni$ - and  $Co$ -rich shell, originating from a corrosion subscale, remained undissolved, even after 22 h of leaching. The leaching mechanism of the interior of such particles was of the “shrinking core” type, in which the leaching rate of REEs was faster than that of  $Ni$ . As dissolution proceeded, this resulted in a concentration gradient inside the core of the particles. These findings highlight the influence of battery anode aging phenomena on the leaching mechanisms of  $Ni$  and REEs from industrial samples of spent NiMH battery powders.

## Experimental Section

### Initial raw material characterization

The BM powder was characterized for chemical content, phase determination, and morphological features. The material was mineralized at 250 °C for 2 h in aqua regia (mixture of  $HCl$  37% and  $HNO_3$  65% in a 1:1 ratio), with a S/L mass ratio of 10%; a cooling system was used to condense vapors. The elemental content was determined by means of ICP-OES (PerkinElmer Optima 8300), for the following elements:  $Al, Cd, Ce, Co, Cu, Fe, La, Li, Mn, Nd, Ni, Pr, Zn, K$ , and  $Na$ . Oxygen and carbon contents were measured by using instrumental gas analyzers (IGAs) equipped with IR detectors (EMGA 620 W LECO for oxygen and EMIA 820 V HORIBA for carbon). Phase composition was determined by means of powder XRD on a D8 BRUKER instrument in the  $\theta/2\theta$  configuration and  $Cu_{K\alpha}$  radiation ( $2\theta$  range of 20–80°, with a wavelength of 1.5418 Å). Cross sections of the solid material were prepared by embedding the powders in a nonconducting thermosetting resin (PolyFast, STRUERS) for hot molding (Mecapress 3, PRESI) and diamond-polished down to 1  $\mu m$  (Mecatech 234, PRESI). Semiquantitative analyses of the cross sections were carried out by using a scanning electron microscope field-emission gun (SEM-FEG, JEOL JSM 7100F) equipped with an EDX Oxford ASDD X-Max detector. Quantitative analyses of the cross sections were performed with an EPMA (CAMECA SXFive FE) equipped with WDS detectors.

### Pilot setup of the leaching experiments

The leaching tests were performed in a 10 L jacketed glass reactor equipped with a three-baffle mechanical stirrer. A constant mixing

rate of 400 rpm ensured the suspension of all particles. The temperature inside the reactor was regulated by using a HUBER Ministat 240 instrument. A mass of 1.2 kg of BM powder was added at a constant rate of 50 g min<sup>-1</sup> in an initial volume of 8 L of demineralized water, leading to an initial S/L ratio of 15%; the starting time ( $t = 0$ ) of the experiment was the beginning of BM addition. The pH of the solution in the reactor was regulated in the range of  $3 < \text{pH} < 5.5$ , by using a PID controller connected to a pump and a stock container of leaching agent. Relative pH standard deviations were lower than  $\pm 4\%$  for all experiments. HCl (12 M/12 N) or H<sub>2</sub>SO<sub>4</sub> (6 M/12 N) were used as leaching agents (reagent grade) for pH adjustment and acid consumption was followed by measuring the mass of acid with a balance. The effects of three process parameters on leaching yields and mechanisms were studied up to 22 h: the influence of pH (3–5.5) at 40 °C in HCl, and the influence of temperature (25–60 °C) and type of acid (HCl or H<sub>2</sub>SO<sub>4</sub>) at pH 3. At the end of the runs, the remaining solid leach residue was filtered from the PLS by using a pneumatic filter press and the PLS was collected for further treatment.

To follow the evolution of the leaching yields, samples (5 mL) were taken at periodic time intervals, filtered through 0.45 µm syringe filters, and analyzed by means of ICP-OES. The resulting leaching yield for a given element,  $i$ , at time  $t$ ,  $LY_i(t)$ , is calculated according to Equation (10):

$$LY_i(t) = 100 \frac{C_i(t)V_{\text{tot}}(t)}{m_{\text{BM}}w_i} \quad (10)$$

in which  $C_i(t)$  is the concentration of element  $i$  in the sample at time  $t$  (in g L<sup>-1</sup>),  $V_{\text{tot}}(t)$  is the total volume of solution (H<sub>2</sub>O + added acid, in L),  $m_{\text{BM}}$  is the initial mass of BM powder (in g), and  $w_i$  is the mass fraction of element  $i$  in the initial BM powder.

In addition, for some experiments, four samples ( $\approx 150$  mL) were extracted at different times and filtered by using a Büchner system, to 1) measure the S/L ratio evolution; and 2) characterize the solid residues by means of XRD, SEM-FEG, EPMA, and ICP-OES. The consistency of the overall elementary mass balance was verified for one set of conditions (H<sub>2</sub>SO<sub>4</sub> (6 M), pH 3, 40 °C, repeated twice) by comparing the analysis of the solid samples extracted with the Büchner system, the analysis of the aqueous solution, and the initial BM composition.

## Thermodynamic calculations

Thermodynamic calculations were carried out thanks to the geochemical software PHREEQC operated with PHREEPlot.<sup>[56]</sup> The extended Debye–Hückel b-dot equation of the LLNL model was used to calculate aqueous activity coefficients.<sup>[56]</sup> Thermodynamic data were taken from the 2017 version of the Thermodynamic database<sup>[57]</sup> and completed to account for the thermodynamic properties of solid phases (La(OH)<sub>3</sub>,<sup>[58]</sup> LaNi<sub>5</sub>,<sup>[59]</sup> and La<sub>2</sub>NiO<sub>4</sub><sup>[41]</sup>) and aqueous lanthanide chloride compounds (LaCl<sub>2</sub><sup>+</sup>, LaCl<sub>2</sub><sup>2+</sup>, LaCl<sub>3</sub>, and LaCl<sub>4</sub>),<sup>[60,61]</sup> valid in the temperature range 25–90 °C.  $E_h$  pH speciation diagrams were calculated at 25, 40, and 60 °C, with La and Ni concentrations corresponding to a 15 wt% S/L ratio (S is the solid BM and L is the HCl–H<sub>2</sub>O liquid phase).

## Acknowledgements

We wish to thank Sophie Gouy and Philippe De Parseval from the Centre de Micro-caractérisation Raimond Castaing for various

EPMA analyses, as well as Marie-Line de Solan-Bethmale from the Laboratoire de Génie Chimique (LGC) for the SEM analyses, and Cédric Charvillat from the Centre Interuniversitaire de Recherche et d'Ingénierie des Matériaux (CIRIMAT) for the powder XRD measurements.

## Conflict of interest

The authors declare no conflict of interest.

**Keywords:** alkali metals • electrochemistry • nanoparticles • nickel • rare earths

- [1] Deloitte Sustainability, British Geological Survey, Minières, Bureau de Recherches Géologiques et Minières, Research, Netherlands Organisation for Applied Scientific, *Study on the Review of the List of Critical Raw Materials*, Brussels, **2017**.
- [2] L. E. O. C. Rodrigues, M. B. Mansur, *J. Power Sources* **2010**, *195*, 3735–3741.
- [3] P. Meshram, B. D. Pandey, T. R. Mankhand, *Waste Manage.* **2016**, *51*, 196–203.
- [4] C. Pillot, *The Rechargeable Battery Market and Main Trends 2016–2025*, **2017**.
- [5] Trinomics, *Study in Support of Evaluation of the Directive 2006/66/EC on Batteries and Accumulators and Waste Batteries and Accumulators*, **2014**.
- [6] European Union, *European Innovation Partnership on Raw Materials: Raw Materials Scoreboard*, **2016**.
- [7] J. J. M. Nelson, E. J. Schelter, *Inorg. Chem.* **2019**, *58*, 979–990.
- [8] ADEME, **2017**, 1–146.
- [9] P. Subir, *Understanding the Material Science of Battery We Use Every Day*, found under <http://www.tsijournals.com/articles/understanding-the-material-science-of-battery-we-use-everyday.html>.
- [10] J. Nan, D. Han, M. Yang, M. Cui, *J. Electrochem. Soc.* **2006**, *153*, A101.
- [11] S. Al Thyabat, T. Nakamura, E. Shibata, A. Iizuka, *Miner. Eng.* **2013**, *45*, 4–17.
- [12] V. Innocenzi, F. Vegliò, *J. Power Sources* **2012**, *211*, 184–191.
- [13] K. Larsson, C. Ekberg, A. Ødegaard Jensen, *Waste Manage.* **2013**, *33*, 689–698.
- [14] A. Porvali, B. P. Wilson, M. Lundström, *Waste Manage.* **2018**, *71*, 381–389.
- [15] K. Young, B. Chao, Y. Liu, J. Nei, *J. Alloys Compd.* **2014**, *606*, 97–104.
- [16] A. Fernandes, J. C. Afonso, A. J. B. Dutra, *Hydrometallurgy* **2013**, *133*, 37–43.
- [17] N. Tzanetakis, K. Scott, *J. Chem. Technol. Biotechnol.* **2004**, *79*, 919–926.
- [18] K. Korkmaz, M. Alemrajabi, Å. C. Rasmuson, K. M. Forsberg, *Metals* **2018**, *8*, 1062.
- [19] P. Zhang, T. Yokoyama, O. Itabashi, Y. Wakui, T. M. Suzuki, K. Inoue, *Hydrometallurgy* **1998**, *50*, 61–75.
- [20] X. Yang, J. Zhang, X. Fang, *J. Hazard. Mater.* **2014**, *279*, 384–388.
- [21] F. Holmberg, *Recycling of Nickel Metal Hydride (NiMH) Batteries: Characterization and Recovery of Nickel, ABS Alloy and Cobalt*, Chalmers University of Technology, **2017**.
- [22] S. Luidold, H. Antrekowitsch, EP 2 444 507 B1, **2012**.
- [23] M. Petranikova, I. Herdžik Koniecko, B. M. Steenari, C. Ekberg, *Hydrometallurgy* **2017**, *171*, 128–141.
- [24] L. Li, S. Xu, Z. Ju, F. Wu, *Hydrometallurgy* **2009**, *100*, 41–46.
- [25] M. A. Rabah, F. E. Farghaly, M. A. Abd El Motaleb, *Waste Manage.* **2008**, *28*, 1159–1167.
- [26] L. Pietrelli, B. Bellomo, D. Fontana, M. R. Monteverdi, *Hydrometallurgy* **2002**, *66*, 135–139.
- [27] L. Pietrelli, B. Bellomo, D. Fontana, M. Monteverdi, *Waste Manage.* **2005**, *25*, 221–226.
- [28] P. Meshram, B. D. Pandey, T. R. Mankhand, *Hydrometallurgy* **2015**, *158*, 172–179.
- [29] D. A. Bertuol, A. M. Bernardes, J. A. S. Tenório, *J. Power Sources* **2009**, *193*, 914–923.

- [30] A. R. Alonso, E. A. Perez, G. T. Lapidus, R. M. Luna Sanchez, *Hydrometallurgy* **2014**, 1, 277–289.
- [31] P. Zhang, T. Yokoyama, O. Itabashi, Y. Wakui, T. M. Suzuki, K. Inoue, *J. Power Sources* **1999**, 77, 116–122.
- [32] C. Liu, Y. Deng, J. Chen, D. Zou, W. Su, *Ind. Eng. Chem. Res.* **2017**, 56, 7551–7558.
- [33] A. Porvali, V. Agarwal, M. Lundström, *Mining, Metall. Explor.* **2019**, 36, 979–991.
- [34] P. Leblanc, B. Knosp, C. Jordy, P. Blanchard, *J. Electrochem. Soc.* **1998**, 145, 860–863.
- [35] P. Bäuerlein, C. Antonius, J. Löffler, J. Kümpers, *J. Power Sources* **2008**, 176, 547–554.
- [36] F. Maurel, B. Knosp, M. Backhaus Ricoult, *J. Electrochem. Soc.* **2000**, 147, 78–86.
- [37] D. Chartouni, F. Meli, A. Züttel, K. Gross, L. Schlapbach, *J. Alloys Compd.* **1996**, 241, 160–166.
- [38] M. Ikoma, K. Komori, S. Kaida, C. Iwakura, *J. Alloys Compd.* **1999**, 284, 92–98.
- [39] X. Zhou, K. Young, J. West, J. Regalado, K. Cherisol, *J. Alloys Compd.* **2013**, 580, S373–S377.
- [40] L. Schlapbach, A. Seiler, H. C. Siegmann, F. Stucki, *J. Less Common Met.* **1980**, 73, 145–160.
- [41] M. Zinkevich, F. Aldinger, *J. Alloys Compd.* **2004**, 375, 147–161.
- [42] S. A. Hosseini, S. Raygan, A. Rezaei, A. Jafari, *J. Environ. Chem. Eng.* **2017**, 5, 3922–3929.
- [43] M. S. Wickleder, *Chem. Rev.* **2002**, 102, 2011–2087.
- [44] P. A. Degtiarev, *J. Less Common Met.* **1979**, 68, 107–110.
- [45] V. Manomenova, E. Rudneva, A. Voloshin, *Russ. Chem. Rev.* **2016**, 85, 585–609.
- [46] A. E. Voloshin, V. L. Manomenova, E. B. Rudneva, N. A. Vasilyeva, V. M. Masalov, A. A. Zhokhov, G. A. Emelchenko, *J. Cryst. Growth* **2018**, 500, 98–103.
- [47] N. A. Vasilyeva, D. Nuzhdin, M. A. Faddeev, V. V. Grebenev, V. A. Lykov, A. E. Voloshin, *Crystallogr. Rep.* **2016**, 61, 304–307.
- [48] E. Santos, P. Hindelang, P. Quaino, E. N. Schulz, G. Soldano, W. Schmickler, *ChemPhysChem* **2011**, 12, 2274–2279.
- [49] T. Du, A. Vijayakumar, K. B. Sundaram, V. Desai, *Microelectron. Eng.* **2004**, 75, 234–241.
- [50] A. E. Sanli, A. Aytac, *ECS Trans.* **2012**, 42, 3–22.
- [51] M. Itagaki, H. Nakazawa, K. Watanabe, K. Noda, *Corros. Sci.* **1997**, 39, 901–911.
- [52] N. Sato, G. Okamoto, *J. Electrochem. Soc.* **1963**, 110, 605–614.
- [53] A. N. Zelikman, O. E. Krein, G. V. Samsonov, *Metallurgy of Rare Metals*, **1964**.
- [54] D. S. Todorovsky, M. M. Milanova, N. L. Minkova, C. Balarev, *Monatsh. Chem.* **1993**, 124, 673–679.
- [55] E. P. Lokshin, O. A. Tareeva, K. G. Ivlev, T. G. Kashulina, *Russ. J. Appl. Chem.* **2005**, 78, 1058–1063.
- [56] D. L. Parkhurst, C. A. J. Appelo, *PHREEQC (Version 3) A Computer Program for Speciation, Batch Reaction, One Dimensional Transport, and Inverse Geochemical Calculations*, **2013**.
- [57] P. Blanc, A. Lassin, P. Piantone, M. Azaroual, N. Jacquemet, A. Fabbri, E. C. Gaucher, *Appl. Geochem.* **2012**, 27, 2107–2116.
- [58] C. Ekberg, P. L. Brown, *Hydrolysis of Metal Ions*, Wiley VCH, Weinheim, **2016**.
- [59] N. P. Gorbachuk, V. B. Muratov, *Powder Metall. Met. Ceram.* **2005**, 44, 467–471.
- [60] J. Haas, E. Shock, D. Sassani, *Geochim. Cosmochim. Acta* **1995**, 59, 4329–4350.
- [61] E. L. Shock, H. C. Helgeson, *Geochim. Cosmochim. Acta* **1988**, 52, 2009–2036.